J. Fluid Mech. (2012), *vol.* 692, *pp.* 369–394. © Cambridge University Press 2012
doi:10.1017/jfm.2011.519

Rotation of spheroidal particles in Couette flows

Haibo Huang[1,2]†‡, Xin Yang[1], Manfred Krafczyk[2] and Xi-Yun Lu[1]

[1] Department of Modern Mechanics, University of Science and Technology of China, Hefei, Anhui 230026, China

[2] Institute for Computational Modelling in Civil Engineering, Technische Universität, Braunschweig 38106, Germany

(Received 15 November 2010; revised 1 October 2011; accepted 21 November 2011; first published online 5 January 2012)

The rotation of a neutrally buoyant spheroidal particle in a Couette flow is studied by a multi-relaxation-time (MRT) lattice Boltzmann method. We find several new periodic and steady rotation modes for a prolate spheroid for Reynolds numbers (Re) exceeding 305. The simulations cover the regime up to $Re \leqslant 700$. The rotational behaviour of the spheroid appears to be not only sensitive to the Reynolds number but also to its initial orientation. We discuss the effects of initial orientation in detail. For $305 < Re < 345$ we find that the prolate spheroid reaches a periodic mode characterized by precession and nutation around an inclined axis which is located close to the middle plane where the velocity is zero. For $345 < Re < 385$, the prolate spheroid precesses around the vorticity direction with a nutation. For Re close to the critical $Re_c \approx 345$, a period-doubling phenomenon is observed. We also identify a motionless mode at higher Reynolds numbers ($Re > 445$) for the prolate spheroid. For the oblate spheroid the dynamic equilibrium modes found are log rolling, inclined rolling and different steady states for Re increasing from 0 to 520. The initial-orientation effects are studied by simulations of 57 evenly distributed initial orientations for each Re investigated. Only one mode is found for the prolate spheroid for $Re < 120$ and $385 < Re < 445$. In other Re regimes, more than one mode is possible and the final mode is sensitive to the initial orientation. However, the oblate spheroid dynamics are insensitive to its initial orientation.

Key words: particle/fluid flows, suspensions

1. Introduction

Suspended particles in flows occur in many applications and play an important role in industry. For example, the behaviour of suspended particles may affect the quality of paper (Qi & Luo 2003). The rotational behaviour of prolate spheroids at very low Reynolds numbers (Re) has been studied theoretically for a long time. Jeffery (1922) investigated the motion of a single ellipsoid in shear flow while completely neglecting inertial effects. He concluded that the final rotational state of an ellipsoid cannot be determined because it depends on initial conditions. To definitively determine the final rotational state, Jeffery (1922) hypothesized that 'The particle will tend to adopt

† Email address for correspondence: huanghb@ustc.edu.cn
‡ Present address: Technische Universität, Braunschweig 38106, Germany.

that motion which, of all the motions possible under the approximated equations, corresponds to the least dissipation of energy'. Extensive analytical investigations (Harper & Chang 1968; Leal 1975) have studied the inertial effect at $Re < 1$ using perturbation theory. However, their analyses are not applicable to large-Re cases. Leal (1980) have reviewed most of the previous relevant theoretical studies. There are also some relevant experimental works in the literature. Taylor (1923) confirmed Jeffery's hypothesis by investigating the orbit of a prolate or oblate spheroid in a Couette flow at a very low Reynolds number. However, Karnis, Goldsmith & Mason (1963) found that the inertial effect at $Re = O(10^{-3})$ is sufficient to make non-spherical particles adopt a motion that is different from Jeffery's hypothesis.

Different numerical methods have also been used to study the motion of particles in flows. Brady & Bossis (1988) adapted the Stokesian dynamics method for simulating the motion of many particles in Stokes flow. However, this method is only applicable to spherical particles and it neglects the inertial term, which may have a significant influence on the motion of particles. For finite-Reynolds-number flows the Navier–Stokes equations have to be solved. Feng & Joseph (1995) simulated the motion of a single ellipse in two-dimensional (2D) creeping flows using a finite-element approach. They confirmed Jeffery's hypothesis at $Re \approx 1$. However, according to the investigation of the energy dissipation at $Re = 0.1$ and $Re = 18$, the numerical results of Qi & Luo (2003) did not support Jeffery's hypothesis. In this work we will first validate our scheme for calculating relative viscosity and then re-evaluate the validity of the hypothesis.

Ding & Aidun (2000) used a lattice Boltzmann method (LBM), to simulate an elliptical cylinder in planar Couette flow and a single oblate spheroid for $Re < 100$ in a three-dimensional (3D) Couette flow. However, in the 3D simulation, the diameter of the oblate spheroid was fixed in the direction of the vorticity axis. They found that beyond a critical Reynolds number $Re_c = 81$, the 3D oblate ellipsoid rotation would stop and the corresponding Re_c for a 2D elliptical cylinder is $\sim$29. Later, experimental results of Zettner & Yoda (2001) confirmed the numerical finding for the 2D elliptical cylinder.

Qi & Luo (2003) studied a prolate and an oblate particulate suspension in a 3D Couette flow for $Re < 467$ by LBM. They identified the following modes: tumbling, precessing and nutating, log rolling and inclined rolling for a prolate spheroid, which are illustrated in figure 1(*a,b,c,d*) respectively. For an oblate spheroid, they identified the log rolling and inclined rolling as Re increases. Yu, Phan-Thien & Tanner (2007) studied the problem for $Re < 256$ using a fictitious domain (FD) method, but the critical transition Re was found to be very different to that of Qi & Luo (2003). Besides the modes mentioned above (Qi & Luo 2003), Yu *et al.* (2007) identified an extra mode for the oblate spheroid, i.e. the motionless mode. They also found that the orbital behaviour of the prolate spheroid is sensitive to the initial orientation. However, only up to two initial orientations of the spheroids were simulated in these studies. The prolate spheroid does not cease to rotate in their studies, which is not consistent with the observations of Ding & Aidun (2000) and Zettner & Yoda (2001).

Here we investigate the rotation of a spheroid in a 3D Couette flow for Reynolds numbers up to 700. The numerical method used in our study is based on the LBM (Ladd 1994*a*,*b*; Aidun, Lu & Ding 1998; Ding & Aidun 2000). Using the LBM to study the motion of solid particles suspended in a fluid was first proposed by Ladd (1994*a*,*b*).

In the LBM approach used in Aidun *et al.* (1998) the non-slip boundary condition on the particle–fluid interface is treated by the simple bounce-back rule

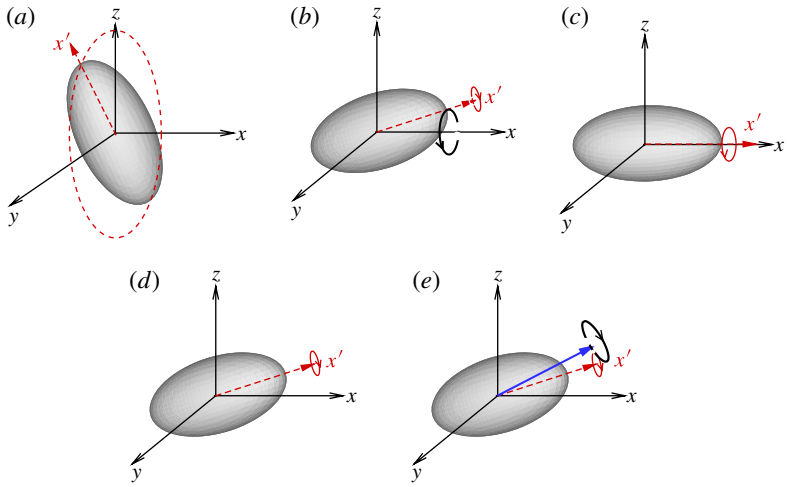

FIGURE 1. (Colour online available at journals.cambridge.org/flm) (*a*) Tumbling mode in the flow-gradient plane (i.e. (y, z)-plane), (*b*) the precessing and nutating mode around the vorticity axis (i.e. x-axis), (*c*) the log-rolling mode, (*d*) the inclined rolling mode, and (*e*) the precessing and nutating mode, around an inclined axis, which is represented by a thick-line arrow. The thin-line circles denote the particle rotating around its evolution axis (x'-axis). The thick-line circles denote precession and nutation.

(He *et al.* 1997; Aidun *et al.* 1998). This treatment requires using a large number of lattice nodes to accurately represent the geometrical boundaries of particles (Feng & Michaelides 2004). Recently, Bouzidi, Firdaouss & Lallemand (2001) proposed a second-order-accurate treatment for moving boundaries based on an accurate curved-wall boundary treatment. In the present study, the fluid flow is solved by the multi-relaxation-time (MRT) LBM proposed by Lallemand & Luo (2003) while the translational and orientational motion of the spheroid is modelled by the Newtonian and Euler equations, respectively.

The present work is intended to provide a better understanding of the rotational behaviour of a non-spherical particle in shear flow. In § 2, the LBM and the basic equations for the motion of the solid particle are introduced briefly. The simulation results for small *Re* are described in § 3. For this regime the results presented in this paper agree well with the theoretical solution of Jeffery (1922) and numerical results obtained by other numerical methods (Yu *et al.* 2007). In §§ 4 and 5, the orientational and rotational behaviours of a prolate and oblate spheroid at different *Re* are reported. The effects of initial orientation are also discussed. In § 6, the validity of Jeffery's hypothesis is examined. Conclusions are presented in § 7.

2. Numerical method

2.1. *MRT lattice Boltzmann equation*

In our study, the fluid flow is solved by the MRT–LBM proposed by Lallemand & Luo (2003). The MRT lattice Boltzmann equation (LBE) is employed to solve the incompressible Navier–Stokes equations. The LBE is (d'Humiéres *et al.* 2002)

$$|f(\boldsymbol{x}+\boldsymbol{e}_i\delta t, t+\delta t)\rangle - |f(\boldsymbol{x}, t)\rangle = -\boldsymbol{M}^{-1}\hat{\boldsymbol{S}}[|m(\boldsymbol{x}, \boldsymbol{t})\rangle - |m^{(eq)}(\boldsymbol{x}, \boldsymbol{t})\rangle], \tag{2.1}$$

i	0	1	2	3	4	5	6	7	8	9	10	11	12	13	14	15	16	17	18
e_{ix}/c	0	1	−1	0	0	0	0	1	−1	1	−1	1	−1	1	−1	0	0	0	0
e_{iy}/c	0	0	0	1	−1	0	0	1	1	−1	−1	0	0	0	0	1	−1	1	−1
e_{iz}/c	0	0	0	0	0	1	−1	0	0	0	0	1	1	−1	−1	1	1	−1	−1

TABLE 1. Discrete velocities of the D3Q19 model.

where the Dirac notation of bra $\langle\cdot|$ and ket $|\cdot\rangle$ vectors symbolize the row and column vectors, respectively. The particle distribution function $|f(\boldsymbol{x},t)\rangle$ has 19 components f_i with $i = 0, 1, 2, 3, \ldots, 18$ in our 3D simulations because the D3Q19 velocity model is used. The collision matrix $\hat{\boldsymbol{S}} = \boldsymbol{M}\cdot\boldsymbol{S}\cdot\boldsymbol{M}^{-1}$ is diagonal with $\hat{\boldsymbol{S}} = \mathrm{diag}(s_0, s_1, \ldots, s_{18})$, and$|m^{(eq)}\rangle$ is the equilibrium value of the moment $|\boldsymbol{m}\rangle$. The matrix $\boldsymbol{M}$ illustrated in the Appendix is a linear transformation which is used to map a vector $|\boldsymbol{f}\rangle$ in discrete velocity space to a vector $|\boldsymbol{m}\rangle$ in moment space, i.e. $|\boldsymbol{m}\rangle = \boldsymbol{M}\cdot|\boldsymbol{f}\rangle$, $|\boldsymbol{f}\rangle = \boldsymbol{M}^{-1}\cdot|\boldsymbol{m}\rangle$.

In the above equation, $\boldsymbol{e}_i$ are the discrete velocities of the D3Q19 model. The three components e_{ix}, e_{iy}, e_{iz} are given in table 1, where c is the lattice speed defined as $c = \delta x/\delta t$. We use the lattice units of $\delta x = 1$ and $\delta t = 1$ in our study.

The macro-variables density ρ and momentum j_ζ are obtained from

$$\rho = \sum_i f_i, \quad j_\zeta = \sum_i f_i e_{i\zeta}, \tag{2.2}$$

where ζ denotes the x, y, or z coordinates. Here the collision process is executed in moment space (d'Humiéres *et al.* 2002). The 19 moments $|\boldsymbol{m}\rangle$ are (d'Humiéres *et al.* 2002)

$$|\boldsymbol{m}\rangle = (\rho, e, \epsilon, j_x, q_x, j_y, q_y, j_z, q_z, 3p_{xx}, 3\pi_{xx}, p_{ww}, \pi_{ww}, p_{xy}, p_{yz}, p_{xz}, m_x, m_y, m_z)^{\mathrm{T}}, \tag{2.3}$$

where e, ϵ, and q_ζ are the energy, the energy squared, and the heat flux, respectively. $(p_{xx}, \pi_{xx}, p_{ww}, \pi_{ww}, p_{xy}, p_{yz}, p_{xz})$ represent stresses and m_x, m_y, m_z are the third-order moments. The equilibria are given by (d'Humiéres *et al.* 2002):

$$e^{(eq)} = -11\rho + \frac{19}{\rho_0} j_\zeta j_\zeta, \quad \epsilon^{(eq)} = w_\epsilon \rho + \frac{w_{\epsilon j}}{\rho_0} j_\zeta j_\zeta, \tag{2.4}$$

$$q_\zeta^{eq} = -\frac{2}{3} j_\zeta, \tag{2.5}$$

$$p_{xx}^{(eq)} = \frac{1}{3\rho_0}[2j_x^2 - (j_y^2 + j_z^2)], \quad p_{ww}^{(eq)} = \frac{1}{\rho_0}[j_y^2 - j_z^2], \tag{2.6}$$

$$p_{xy}^{(eq)} = \frac{1}{\rho_0} j_x j_y, \quad p_{yz}^{(eq)} = \frac{1}{\rho_0} j_y j_z, \quad p_{xz}^{(eq)} = \frac{1}{\rho_0} j_x j_z, \tag{2.7}$$

$$\pi_{xx}^{(eq)} = w_{xx} p_{xx}^{(eq)}, \quad \pi_{ww}^{(eq)} = w_{xx} p_{ww}^{(eq)}, \tag{2.8}$$

$$m_x^{(eq)} = m_y^{(eq)} = m_z^{(eq)} = 0, \tag{2.9}$$

where ρ_0 is the average density of the fluid, and w_ϵ, $w_{\epsilon j}$, and w_{xx} are free parameters which are set to $w_\epsilon = 3$, $w_{\epsilon j} = -11/2$, and $w_{xx} = -1/2$ in our simulations. The

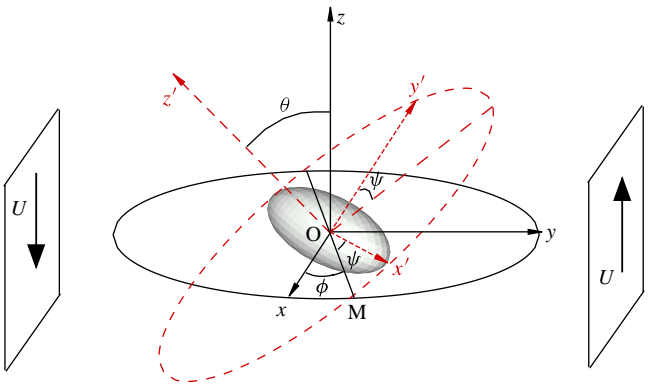

FIGURE 2. (Colour online) Schematic diagram of a spheroid with its symmetry axis in the x'-direction in a Couette flow. Line OM represents the intersection of the (x, y) and the (x', y') coordinate planes. The two walls at $y = 0$ and $y = N_y$ move in opposite directions. Periodic boundary conditions are applied in the x- and z-directions.

diagonal collision matrix $\hat{\boldsymbol{S}}$ is given by (d'Humiéres *et al.* 2002)

$$\hat{\boldsymbol{S}} \equiv \mathrm{diag}(0, s_1, s_2, 0, s_4, 0, s_4, 0, s_4, s_9, s_{10}, s_9, s_{10}, s_{13}, s_{13}, s_{13}, s_{16}, s_{16}, s_{16}). \quad (2.10)$$

The parameters are chosen as: $s_1 = 1.19$, $s_2 = s_{10} = 1.4$, $s_4 = 1.2$, $s_9 = 1/\tau$, $s_{13} = s_9$, and $s_{16} = 1.98$. The parameter τ is related to the kinematic viscosity of the fluid with $\nu = c_s^2(\tau - 0.5)\delta t$ and $c_s = c/\sqrt{3}$. The pressure in the flow field can be obtained from the density via the equation of state $p = c_s^2\rho$.

2.2. *Kinematic equation of the particle*

The translation of the solid particle is determined by solving Newton's equation

$$m\frac{\mathrm{d}\boldsymbol{U}(t)}{\mathrm{d}t} = \boldsymbol{F}(t), \quad (2.11)$$

where m is the mass of the suspended particle and $\boldsymbol{F}$ is the total force acting on the particle.

The rotation of the spheroid is determined by the Euler equation, which is written as

$$\boldsymbol{I} \cdot \frac{\mathrm{d}\boldsymbol{\Omega}(t)}{\mathrm{d}t} + \boldsymbol{\Omega}(t) \times [\boldsymbol{I} \cdot \boldsymbol{\Omega}(t)] = \boldsymbol{T}(t), \quad (2.12)$$

where $\boldsymbol{I}$ is the inertial tensor. Noted that in the body-fixed coordinate system (coordinates (x', y', z') in figure 2), the tensor is diagonal and the principal moments of inertia are $I_{x'x'} = m(b^2 + c^2)/5$, $I_{y'y'} = m(a^2 + c^2)/5$ and $I_{z'z'} = m(a^2 + b^2)/5$, where a, b and c are the lengths of three semi-principal axes of a spheroid in the x'-, y'- and z'-direction, respectively. $\boldsymbol{\Omega}$ represents angular velocity and $\boldsymbol{T}$ are the torques exerted on the solid particle in the same coordinate system. We note here that a simple first-order forward Euler integration procedure may not give accurate results.

It is not appropriate to solve the equation directly due to an inherent singularity (Qi 1999). Thus four quaternion parameters are used as generalized coordinates to solve the corresponding system of equations. The quaternion parameters are defined as $q_0 = \cos\frac{1}{2}\theta\cos\frac{1}{2}(\phi + \psi)$, $q_1 = \sin\frac{1}{2}\theta\cos\frac{1}{2}(\phi - \psi)$, $q_2 = \sin\frac{1}{2}\theta\sin\frac{1}{2}(\phi - \psi)$, $q_3 = \cos\frac{1}{2}\theta\sin\frac{1}{2}(\phi + \psi)$, where (ϕ, θ, ψ) are Euler angles. The coordinate transformation

matrix from the space-fixed frame to the body-fixed frame can be written as

$$\begin{pmatrix} q_0^2+q_1^2-q_2^2-q_3^2 & 2(q_1q_2+q_0q_3) & 2(q_1q_3-q_0q_2) \\ 2(q_1q_2-q_0q_3) & q_0^2-q_1^2+q_2^2-q_3^2 & 2(q_2q_3+q_0q_1) \\ 2(q_1q_3+q_0q_2) & 2(q_2q_3-q_0q_1) & q_0^2-q_1^2-q_2^2+q_3^2 \end{pmatrix}. \tag{2.13}$$

With the quaternion formulation the angular velocity $\boldsymbol{\Omega}$ in (2.12) can be solved together with the following equation to obtain the transformation matrix (Qi 1999):

$$\begin{pmatrix} \dot{q}_0 \\ \dot{q}_1 \\ \dot{q}_2 \\ \dot{q}_3 \end{pmatrix} = \frac{1}{2}\begin{pmatrix} q_0 & -q_1 & -q_2 & -q_3 \\ q_1 & q_0 & -q_3 & q_2 \\ q_2 & q_3 & q_0 & -q_1 \\ q_3 & -q_2 & q_1 & q_0 \end{pmatrix}\begin{pmatrix} 0 \\ \Omega_{x'} \\ \Omega_{y'} \\ \Omega_{z'} \end{pmatrix}. \tag{2.14}$$

In this study, (2.12) and (2.14) are solved using a fourth-order-accurate Runge–Kutta integration procedure.

2.3. *Fluid–solid coupling*

The fluid–solid coupling in our study is based on the scheme of Lallemand & Luo (2003) and Aidun *et al.* (1998).

First we would like to introduce the curved-wall boundary condition briefly. In the study of Aidun *et al.* (1998), the wall is always assumed to be located at the middle of the link between a fluid node and a solid node. However, such an assumption would alter the curved-wall geometry on the grid level. It may also degrade the accuracy of the simulation at finite and higher Reynolds number (Mei *et al.* 2002). Here the accurate moving-boundary treatment proposed by Lallemand & Luo (2003) is adopted. In the scheme the wall location at the link between a fluid node and a solid node is determined by the curved-wall geometry exactly. The fraction in the fluid region of a grid space intersected by the boundary varies from zero to unity. The target of the scheme (Lallemand & Luo 2003) is to obtain $f_{\bar{i}}(\boldsymbol{x}_b+\boldsymbol{e}_{\bar{i}},t)$ accurately, where $f_{\bar{i}}$ is the distribution function of the velocity $\boldsymbol{e}_{\bar{i}}\equiv-\boldsymbol{e}_i$ after streaming. $\boldsymbol{x}_b$ is a solid boundary node (SBN), which means a node inside the solid regime but it has at least one link in direction $\boldsymbol{e}_{\bar{i}}$ connecting to a fluid node. The main idea of the treatment is using Lagrange interpolation to obtain unknown distribution functions and extrapolation is avoided to improve numerical stability (Bouzidi *et al.* 2001).

According to the studies of Mei *et al.* (2002) and Lallemand & Luo (2003), the force on an SBN ($\boldsymbol{x}_b$) is calculated through the momentum exchange scheme (Mei *et al.* 2002):

$$F^{(b)}\left(\boldsymbol{x}_b, t+\tfrac{1}{2}\right) = \sum_i \boldsymbol{e}_i[f_i(\boldsymbol{x}_b,t)+f_{\bar{i}}(\boldsymbol{x}_b+\boldsymbol{e}_{\bar{i}},t)]\times[1-w(\boldsymbol{x}_b+\boldsymbol{e}_{\bar{i}},t)], \tag{2.15}$$

where $w(\boldsymbol{x},t)$ is a scalar array. If the lattice site $\boldsymbol{x}$ is occupied by fluid at time t, $w(\boldsymbol{x},t)=0$; if it is inside the solid body, $w(\boldsymbol{x},t)=1$. Hence, in fact the summation is over all the links connecting to fluid nodes.

However, in the scheme of Lallemand & Luo (2003), they did not consider the force due to the fluid particle entering and leaving the solid region (Aidun *et al.* 1998). Here this force contribution (Aidun *et al.* 1998) is involved.

At time step t, suppose a solid node becomes a fluid node, then the momentum of the solid node would convert to momentum of the fluid, and vice versa. The

calculation of the forces due to momentum given to and taken from the particle is illustrated in the following.

An impulse force would be applied to the particle due to the momentum given to the particle (a fluid node $\boldsymbol{x}$ becomes a solid particle). The force is given by (Aidun *et al.* 1998)

$$\boldsymbol{F}^{(c)}\left(\boldsymbol{x}, t+\tfrac{1}{2}\right)=\sum_{i} f_i(\boldsymbol{x}, t)\boldsymbol{e}_i. \tag{2.16}$$

The momentum lost from the particle (a solid node $\boldsymbol{x}$ becomes a fluid node) is calculated by (Aidun *et al.* 1998; Qi 1999)

$$\rho(\boldsymbol{x}, t)\boldsymbol{u}(\boldsymbol{x}, t)=\rho(\boldsymbol{x}, t)\{\boldsymbol{U}(t)+\boldsymbol{\Omega}(t)\times[\boldsymbol{x}-\boldsymbol{X}(t)]\}, \tag{2.17}$$

where $\boldsymbol{U}(t)$, $\boldsymbol{X}(t)$ are the velocity vector and position of the particle, respectively. Here $\rho(\boldsymbol{x}, t)$ is the density of the newly uncovered fluid node and can be assigned either as a locally averaged density (Aidun *et al.* 1998) or as the averaged density of the whole fluid ρ_0 (Lallemand & Luo 2003). In our simulations, these schemes produce similar results. The force due to the newly uncovered solid nodes is calculated by (Aidun *et al.* 1998; Qi 1999)

$$\boldsymbol{F}^{(u)}(\boldsymbol{x}, t+\tfrac{1}{2})=-\rho(\boldsymbol{x}, t)\boldsymbol{u}(\boldsymbol{x}, t). \tag{2.18}$$

To implement the collision and streaming procedure, the distribution functions f_i of a newly uncovered fluid node should be initialized. Two schemes are applicable. The f_i can be extrapolated through the nearby fluid node (Lallemand & Luo 2003) or the equilibrium distribution functions for f_i can just be computed, i.e.

$$f_i=f_i^{eq}=\omega_i\rho\left\{1+\frac{e_{i\zeta}u_\zeta}{c_s^2}+\frac{e_{i\zeta}u_\zeta e_{i\delta}u_\delta}{2c_s^4}-\frac{u_\zeta u_\zeta}{2c_s^2}\right\} \tag{2.19}$$

(Lallemand & Luo 2003). Our study shows that the two schemes produce similar results, which is consistent with the conclusion in the study of Lallemand & Luo (2003).

The total force on the solid particle at time $t+1/2$ is given by (Aidun *et al.* 1998)

$$\boldsymbol{F}\left(t+\tfrac{1}{2}\right)=\sum_{SBN} F^{(b)}\left(\boldsymbol{x}_b, t+\tfrac{1}{2}\right)+\sum_{CN}\boldsymbol{F}^{(c)}\left(\boldsymbol{x}, t+\tfrac{1}{2}\right)+\sum_{UN}\boldsymbol{F}^{(u)}\left(\boldsymbol{x}, t+\tfrac{1}{2}\right), \tag{2.20}$$

where CN and UN denote the covered nodes and the uncovered nodes, respectively. The torque on the solid particle can be calculated similarly to that in study of Aidun *et al.* (1998). The total force and torque at time t are averaged by those at time $t-1/2$ and $t+1/2$ (Aidun *et al.* 1998).

2.4. *Velocity boundary condition*

For the velocity boundary condition, the non-equilibrium extrapolation scheme is used (Guo, Zheng & Shi 2002). Extension of the scheme is illustrated below. In the scheme, the unknown post-collision moments $|m^+(\boldsymbol{x}_b, t)\rangle$ of a node $\boldsymbol{x}_b$ on the moving wall are decomposed into two components: an equilibrium and a non-equilibrium part. The equilibrium part is obtained from (2.4)–(2.9). In the equations, the velocity is specified and the density of a wall node $\rho(\boldsymbol{x}_b)$ is obtained through extrapolation. It can be simply specified as $\rho(\boldsymbol{x}_b)=\rho(\boldsymbol{x}_b^-)$; $\boldsymbol{x}_b^-$ denotes a fluid node very near to the wall node. For example, if the node indices for $\boldsymbol{x}_b$ on the right wall are (i, j_{max}, k), the node

indices for $\boldsymbol{x}_b^-$ are $(i, j_{max} - 1, k)$. The unknown non-equilibrium part is also obtained through extrapolation. Finally, for a node $(\boldsymbol{x}_b)$ on the left or right moving walls (refer to figure 2), the post-collision unknown moments $|m^+(\boldsymbol{x}_b, t)\rangle$ are

$$|m^+(\boldsymbol{x}_b, t)\rangle = |m^{(eq)}\rangle + [|m^+(\boldsymbol{x}_b^-, t)\rangle - |m^{(eq)}(\boldsymbol{x}_b^-, t)\rangle]. \tag{2.21}$$

Note that the above equation should be implemented after the collision step for all inner fluid nodes has been implemented.

3. Validation of the numerical method

In our study, the prolate or oblate spheroid is described by

$$\frac{x'^2}{a^2} + \frac{y'^2}{b^2} + \frac{z'^2}{c^2} = 1, \tag{3.1}$$

where (x', y', z') represents the body-fixed coordinate system. Euler angles (ϕ, θ, ψ) are used to describe the rotation of the particle. The spatial orientation of any body-fixed frame (coordinate system) can be obtained by a composition of rotations around the (z', x', z')-axis with the above Euler angles from an arbitrary frame of reference (space-fixed frame). The composition of rotations is illustrated in figure 2 and described below. Suppose that the body-fixed coordinates are initially overlapping with the space-fixed coordinate system (x, y, z), and the symmetry axis of the spheroid is in the x'-direction. First the particle rotates around the z'-axis with a polar angle ϕ and then the particle rotates around the new x'-axis with an angle θ. Finally the particle rotates around the z'-axis with an angle ψ. In the space-fixed coordinates, the streamwise direction of the Couette flow is along the z-direction. The velocity gradient and the vorticity are oriented in the y- and x-direction, respectively. Two walls located at $y = 0$ and $y = N_y$ move in opposite directions with speed U as shown in figure 2. Periodic boundary conditions are applied in both the x- and z-direction. The particle Reynolds number is defined as

$$Re = \frac{4Gd^2}{\nu}, \tag{3.2}$$

where the shear rate is defined as $G = 2U/N_y$, d is the length of the semi-major axis (i.e. $d = a$ for the prolate spheroid and $d = b = c$ for the oblate spheroid) and ν is the kinematic viscosity.

In all of our numerical tests, the initial velocity field was initialized as a Couette flow with a uniform pressure field ($p_0 = c_s^2 \rho_0$). The particle is released at the centre of the computational domain with zero velocity. Although the translational motion of the particle is not constrained, the spheroid centre is not found to depart from the centre of the computational domain in all simulated cases.

To validate our simulation, a case of an oblate spheroid rotating in a shear flow (Aidun *et al.* 1998) is simulated. In our simulation, the computational domain is $N_x \times N_y \times N_z = 40 \times 80 \times 110$, and a, b, c of the oblate spheroid particle are 8, 16, 16, respectively. The initial orientation of the particle is $(\phi_0, \theta_0, \psi_0) = (90°, 90°, 90°)$, which means that the evolution axis is parallel to the velocity direction of the two moving walls. The results are illustrated in figure 3. From figure 3(*a*), we can see that the tumbling periods of $Re = 50$ and $Re = 70$ are different and the oblate spheroid would stop when $Re = 90$. The transition of the critical Reynolds number Re_c from the tumbling state to the stationary state is found ~80. The tumbling period as a function of Re predicted by the scaling law is $T = C\,(Re_c - Re)^{-1/2}$ (figure 3*b*), where $Re_c = 80$

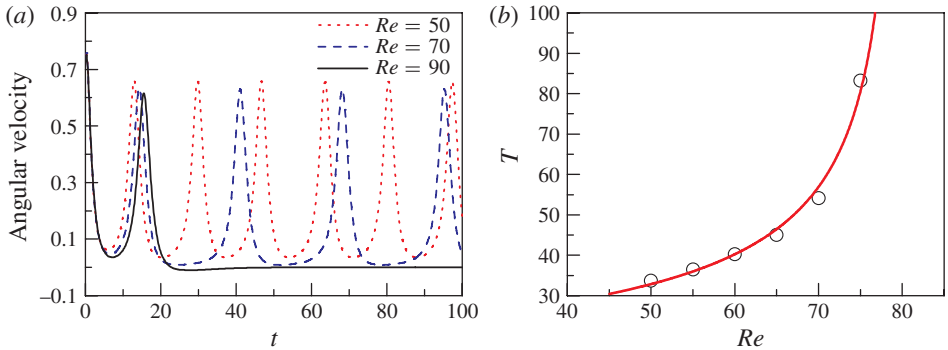

FIGURE 3. (Colour online) (*a*) The angular velocity as a function of the non-dimensional time. (*b*) The tumbling period of the oblate spheroid as a function of Reynolds number. The circles are results of LBM simulations. The prediction (i.e., the solid line) of the scaling law is $T = C\,(Re_c - Re)^{-1/2}$, where $Re_c = 80$ and $C \approx 180$, which agrees well with the simulated results.

and $C \approx 180$, very consistent with that predicted by Aidun *et al.* (1998) with $Re_c = 81$ and $C = 200$.

To further validate our numerical method, LBM simulations are performed to compare the analytical solution of the so-called Jeffery orbit (Jeffery 1922) and results obtained by another numerical method (Yu *et al.* 2007). In these simulations, the mesh size is $96 \times 96 \times 96$ and $Re = 0.5$. The confinement ratio is $r_1 = N_y/a = 8$ and the aspect ratio of the prolate spheroid (major diameter over minor diameter) is $r_2 = a/b = 2$. The effect of the confinement ratio on the rotation of the spheroid will be discussed at the end of § 4.1. In order to compare our results with Jeffery's analytical solution, the initial orientation is set as $(\phi_0, \theta_0, \psi_0) = (90°, 0°, 0°)$, which makes the particle quickly enter a tumbling mode. *Tumbling* here implies a particle rotation about its minor axis and the minor axis is parallel to the vorticity direction. The criterion to identify a stable tumbling mode is $(|T(n) - T(n-1)|)/T(n) < 0.0005$, where $T(n)$ is the period of the nth cycle.

For a stable mode, the period does not change in time after some transient. During the first two periods ($t < 31.5$) the tumbling mode already seems to have been reached because $(|T(2) - T(1)|)/T(2) = 0.000\,35$. We note for clarity that in all the LBM results, the time and the angular velocity are non-dimensionalized by a scaling with $1/G$ and G, respectively.

In figure 4(*a*) ω_x is shown as function of time. The period obtained from LBM is $T = 15.670$ and that obtained from Jeffery's analytical solution is $T = 15.708$. The deviation between the results of LBM and the analytical ones is $\sim$0.24 %. Hence, the LBM result at $Re = 0.5$ is very consistent with the analytical one. In figure 4(*b*) we show directional cosine curves obtained by the LBM and the FD method (Yu *et al.* 2007) during the first two periods. In this simulation, the particle's initial orientation is $(\phi_0, \theta_0, \psi_0) = (0°, 90°, 45°)$; α, β and γ here denote the angles between the x'-axis and the space-fixed coordinates x-, y-, and z-axes, respectively ($\cos^2\alpha + \cos^2\beta + \cos^2\gamma = 1$). The result obtained by the LBM also agrees well with the numerical result obtained by the FD method (Yu *et al.* 2007). It is noted that after a few periods, the rotational mode for this case is also tumbling.

We also studied the confinement ratio effect on the rotation of the spheroid at low Re. For $r_1 = 4$ and identical Re, r_2 and mesh resolution, the period obtained from

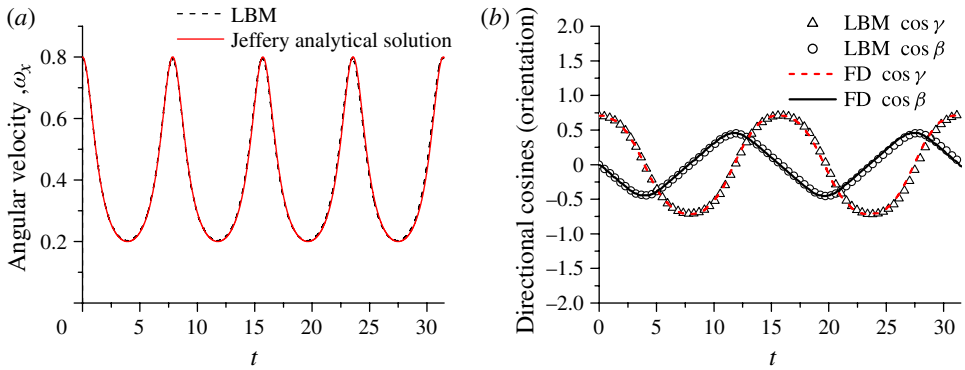

FIGURE 4. (Colour online) Rotational and orientational behaviour of a prolate spheroid at $Re = 0.5$, $r_1 = 8$ and $r_2 = 2$: (*a*) angular velocity as a function of time obtained by LBM and Jeffery's analytical solution, the initial orientation $(\phi_0, \theta_0, \psi_0) = (90°, 0°, 0°)$; (*b*) the directional cosines as functions of time obtained by LBM simulation and the FD method (Yu *et al.* 2007) for $(\phi_0, \theta_0, \psi_0) = (0°, 90°, 45°)$.

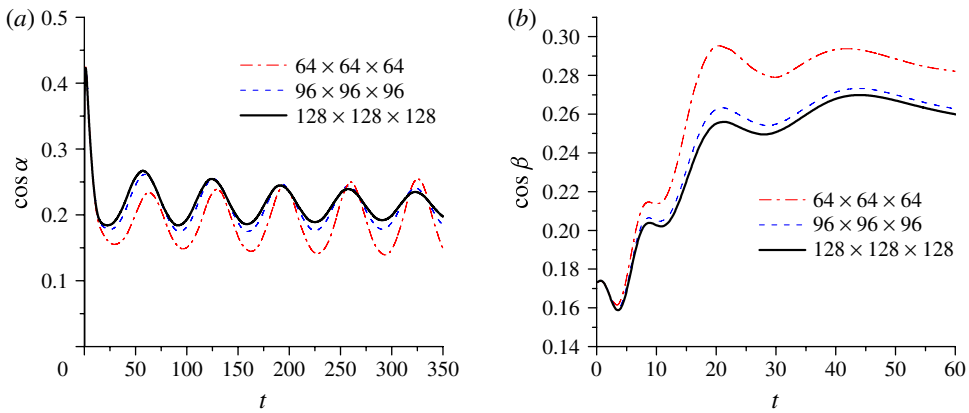

FIGURE 5. (Colour online) Grid independence study for the rotation of a prolate spheroid with $Re = 300$ (*a*) and $Re = 600$ (*b*). In both cases, the initial orientation is $(\phi_0, \theta_0, \psi_0) = (5°, 5°, 5°)$.

simulation is 2.6 % larger than the analytical one. Since the analytical solution is only applicable to cases with large r_1, if r_1 is not large enough the two confined moving boundaries at $y = 0$ and $y = N_y$ would slightly affect the period of rotation.

The mesh of the computational domain in all of our following simulations is $N_x \times N_y \times N_z = 96 \times 96 \times 96$. To check whether this resolution is reasonable, a grid-convergence study was carried out for rotation of a prolate spheroid with $Re = 300$ and 600. The directional cosines obtained by different meshes for the two cases are illustrated in figure 5. In all of the simulations, $r_1 = 4$, $r_2 = 2$ and $U = 0.1$ (in units $\mathrm{d}x/\mathrm{d}t$). In both cases, we can see that the results obtained by mesh $64 \times 64 \times 64$ show a relatively large discrepancy with those obtained by $128 \times 128 \times 128$. The results of mesh $96 \times 96 \times 96$ are very close to those of mesh $128 \times 128 \times 128$. Hence, in the Reynolds number range we studied ($Re < 700$), the mesh size $96 \times 96 \times 96$ seems sufficient to obtain accurate results. To investigate the compressibility effect of

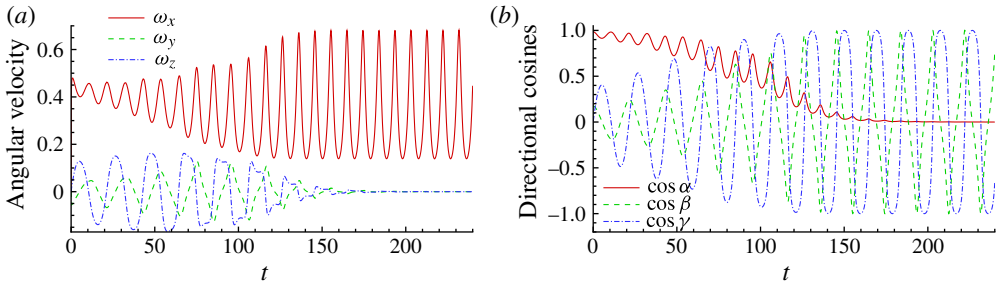

FIGURE 6. (Colour online) The rotational behaviour of the prolate spheroid at $Re = 50$. The angular velocity $\boldsymbol{\omega} = (\omega_x, \omega_y, \omega_z)$ (*a*) and orientation (*b*) as functions of time.

LBM with $U = 0.1$, we also simulated the case $Re = 300$ with $U = 0.06$, and found no significant differences between the results for $U = 0.1$ and $U = 0.06$. Hence, the compressibility effect is relatively small. In order to accelerate the computations we thus chose a velocity $U = 0.1$.

4. Rotation and orientation of a prolate spheroid

4.1. *Effects of Reynolds number*

First, we study the effects of Reynolds number on the final mode of the prolate spheroid. In our numerical settings, the computational domain is $96 \times 96 \times 96$ and $a = 24$, $b = 12$ and $c = 12$. The confinement ratio is $N_y/a = 4$ and the prolate spheroid aspect ratio is $r_2 = 2$. The following results are based on the initial orientation $(\phi_0, \theta_0, \psi_0) = (5°, 5°, 5°)$ implying a slight deviation of the particle's axis of symmetry with respect to the vorticity axis. Our results show that there are *seven* rotational transitions and *eight* steady or periodic modes in the range $0 < Re < 700$. We estimate the error of the critical Re separating these regimes to be $\sim \pm 5$ because we chose an increment of $\Delta Re \approx 10$ in the simulations. For example, if two cases with $Re = 230$ and $Re = 240$ have different rotational modes, $Re_c = 235$ is assigned to separate the different regimes. In order to identify the final mode we define a criterion $(|T(n) - T(n-1)|)/T(n) < 0.0005$, where $T(n)$ denotes the period T of $\omega_x(t)$ in the nth cycle. If $\omega_x(t)$ does not change periodically, we used the following criterion to identify the final steady mode $(|\omega_x(t) - \omega_x(t - 1000)|)/\omega(t) < 0.0005$, where t is the time step. The different regimes labelled from (i) to (viii) are discussed below.

(i) Regime one ($0 < Re < 120$).

In this low-Reynolds-number range, the prolate spheroid reaches the tumbling mode. The angular velocities $\boldsymbol{\omega} = (\omega_x, \omega_y, \omega_z)$ as functions of time are shown in figure 6(*a*). We observe that in equilibrium ω_x changes periodically in time while ω_y and ω_z are zero. To describe the tumbling mode in more detail, $\cos\alpha$, $\cos\beta$, $\cos\gamma$ as functions of time are shown in figure 6(*b*). We observe that eventually $\cos\alpha = 0$ and $\cos\beta$ and $\cos\gamma$ vary from -1 to 1, which means that the x'-axis is always perpendicular to the x-axis and the spheroid is rotating in the (y, z)-plane.

(ii) $Re \approx 120$.

The major axis of the spheroid (x'-axis) precesses around the vorticity axis (x-axis) with a nutation. This mode is illustrated in figure 1(*b*). From figure 7, we can see that the three components of the angular velocity $\boldsymbol{\omega}$ are periodic in time and ω_y and ω_z change periodically in the range $(-0.05, 0.05)$ and $(-0.15, 0.15)$, respectively. $\cos\alpha$, $\cos\beta$, $\cos\gamma$ as functions of time are shown in figure 7(*b*). We

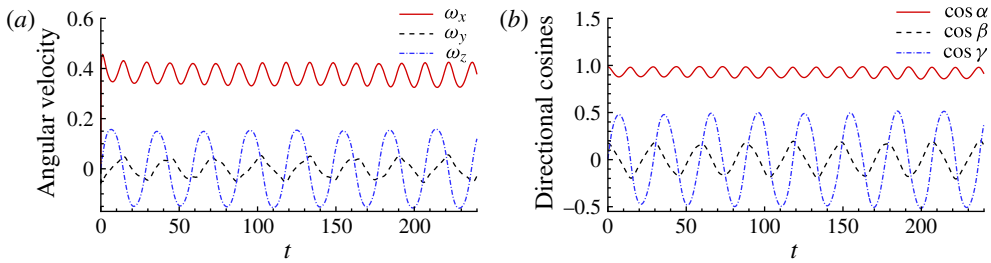

FIGURE 7. (Colour online) The precessing and nutating mode of the prolate spheroid at $Re = 120$. The angular velocity $\boldsymbol{\omega} = (\omega_x, \omega_y, \omega_z)$ (*a*) and orientation (*b*) as functions of time.

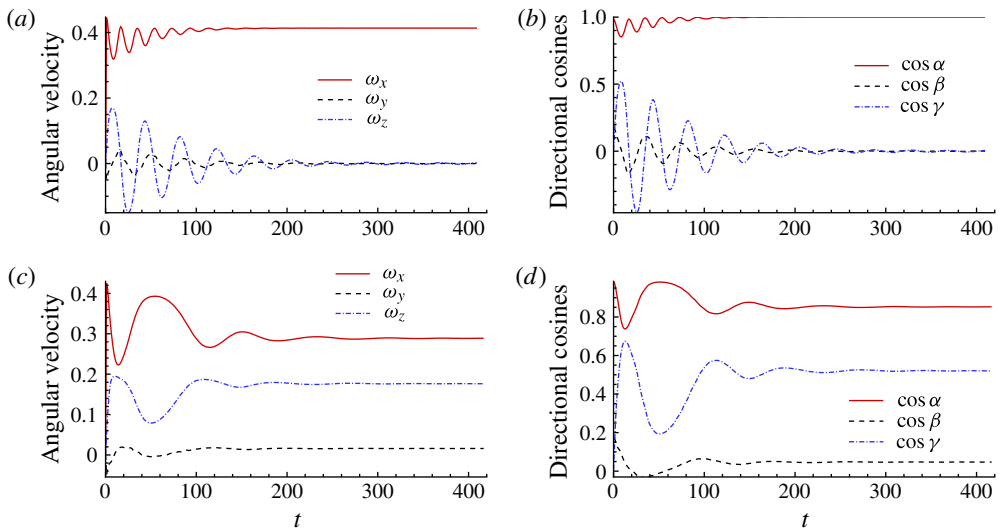

FIGURE 8. (Colour online) (*a*) Transient angular velocity and (*b*) orientation at $Re = 160$ with $(\phi_0, \theta_0, \psi_0) = (5°, 5°, 5°)$. The mode for this Re is termed log rolling. (*c*) Transient angular velocity and (*d*) orientation at $Re = 270$ with initial orientation $(5°, 5°, 5°)$. The mode at this Re is termed inclined rolling.

observe that $-0.20 < \cos\beta < 0.20$ and $-0.50 < \cos\gamma < 0.50$, which means that the nutation amplitude in the z-direction is larger than that in the y-direction.

(iii) Regime two ($120 < Re < 235$).

The spheroid eventually rotates around its axis of symmetry, which is along the x-direction with a constant rate. This is shown in figure 1(*c*). For a typical case of $Re = 160$, the angular velocities as functions of time are shown in figure 8(*a*); ω_y and ω_z are almost equal to zero at equilibrium. Figure 8(*b*) shows $\cos\alpha = 1$, $\cos\beta = 0$ and $\cos\gamma = 0$ as a typical case for a mode called 'log rolling' (Yu *et al.* 2007).

(iv) Regime three ($235 < Re < 305$).

In this regime the dynamic equilibrium of the prolate spheroid can be described by the 'inclined rolling' mode (Yu *et al.* 2007). Here the particle rotates around its axis of symmetry, which almost stays in the (x, z)-plane. This is illustrated in figure 1(*d*). We observe that $\alpha \neq 0$. Figure 8(*c,d*) shows a typical result in this regime for $Re = 270$. Eventually the vector $\boldsymbol{\omega}$ becomes constant. The x'-axis is found to be located almost in

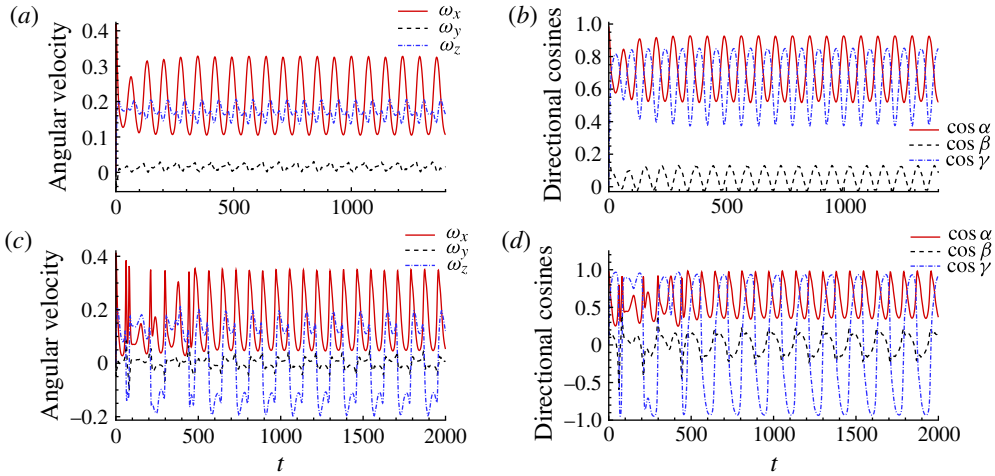

FIGURE 9. (Colour online) (*a*) Transient angular velocity and (*b*) orientation at $Re = 320$ with initial orientation $(5°, 5°, 5°)$. The equilibrium mode for this Re is precessing and nutating around an inclined axis. (*c*) Transient angular velocity and (*d*) orientation at $Re = 380$ with initial orientation $(5°, 5°, 5°)$. The periodic mode is precessing and nutating around the x-axis.

the (x, z)-plane because $\cos\beta \approx 0$. For this case the angle between x' and x is $\sim 31.4°$ because we can read from figure 8(*d*) that $\cos\alpha = 0.853$. This mode was also reported in Yu *et al.* (2007) but not in Qi & Luo (2002, 2003).

(v) Regime four ($305 < Re < 345$).

The x'-axis of the prolate spheroid will precess around an inclined axis with a nutation. This mode is illustrated in figure 1(*e*). In the figure the orientation of the inclined axis is shown as a thick-line arrow. A typical result for this regime for $Re = 320$ is shown in figure 9(*a,b*). Although the angular velocity ω_z as a function of time is periodic, it is more complex than a simple sinusoidal function. The periodic rotational behaviour is more complex than the simple precessing and nutating at $Re \approx 120$. Figure 9(*b*) shows that the inclined axis stays almost in the (x, z)-plane because the x'-axis is almost perpendicular to the y-axis ($\cos\beta \approx 0$). The orientation of the inclined axis can be calculated from figure 9(*b*) by averaging the directional cosines over time. In this case the angle between the inclined axis and the x-axis is found to stay below 45°.

(vi) Regime five ($345 < Re < 385$).

A typical result in this regime for $Re = 380$ is shown in figures 9(*c*) and 9(*d*). We observe that in equilibrium the prolate spheroid precesses around the x-axis with a nutation again. However, there are many frequencies appearing in the corresponding time series of ω_x, ω_y and ω_z instead of a single frequency in the case of $Re \approx 120$. Hence, the precession and nutation are more complex than at $Re \approx 120$. In the present case, the nutation amplitude in the z-direction is much larger than that in the y-direction.

Clearly, the spectrum of $\omega_x(t)$ in regimes four and five deserves special attention. In figure 10 we show $\boldsymbol{\omega}(t)$ for $Re = 340$ and 350, which are close to the transient $Re_c \approx 345$. Obviously there are substantial differences from the cases with $Re = 320$ and 380 which seem to be related to a period-doubling scenario. The corresponding results of a Fourier analysis are listed in table 2. When Re increases from 310 to 340,

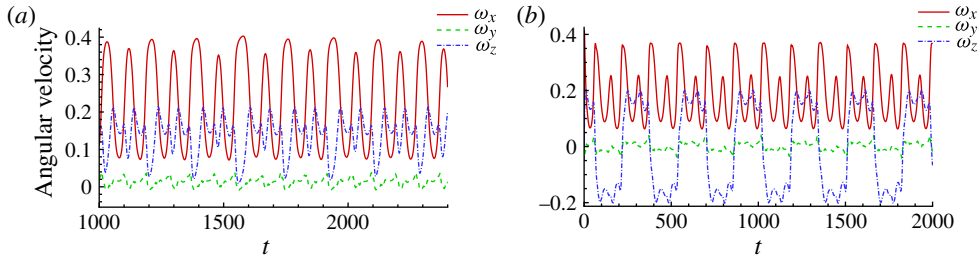

FIGURE 10. (Colour online) $\boldsymbol{\omega}$ components as functions of time at $Re = 340$ (*a*) and 350 (*b*).

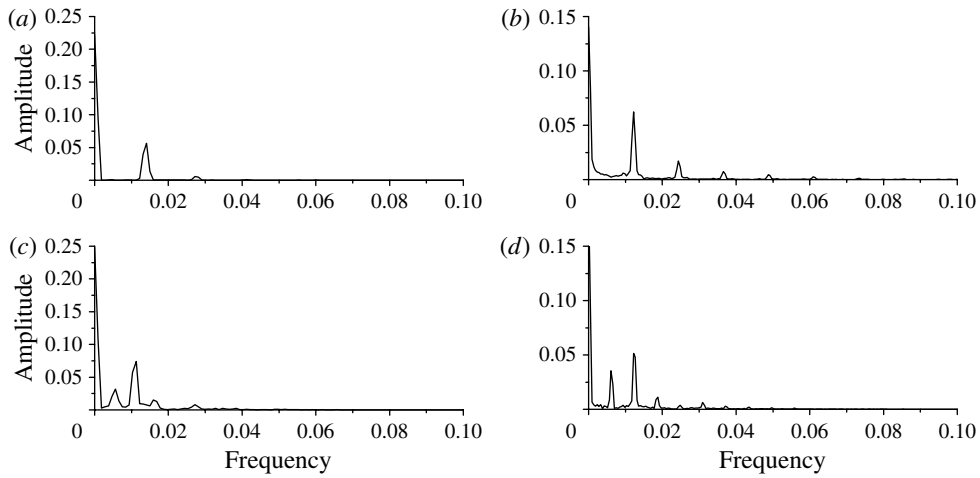

FIGURE 11. Frequency distribution and amplitude of $\omega_x(t)$ at $Re = 320$ (*a*), 380 (*b*), 340 (*c*) and 350 (*d*).

Regime	Re	Main frequency (f_0)	Note
4	310	0.0147	—
4	320	0.0136	—
4	330	0.0127	—
4	340	0.0113	$f_0/2$ appears
5	350	0.0124	$f_0/2$ appears
5	380	0.0122	—

TABLE 2. Main frequency of ω_x for regimes four and five.

the main frequency of $\omega_x(t)$ decreases monotonically from 0.0147 to 0.0113. For the two cases in regime five $Re = 350$ and 380, the main frequencies are almost identical. Figure 11 shows the detailed results of Fourier analysis using a Hamming window function for $\omega_x(t)$ at $Re = 320$, 380, 340, 350. It is found that at $Re = 340$ and 350 in addition to the main frequency f_0 a new independent frequency $f_0/2$ appears. This indicates that the period-doubling phenomenon appears at $Re = 340$ and 350 compared to $Re = 320$ and 380, respectively.

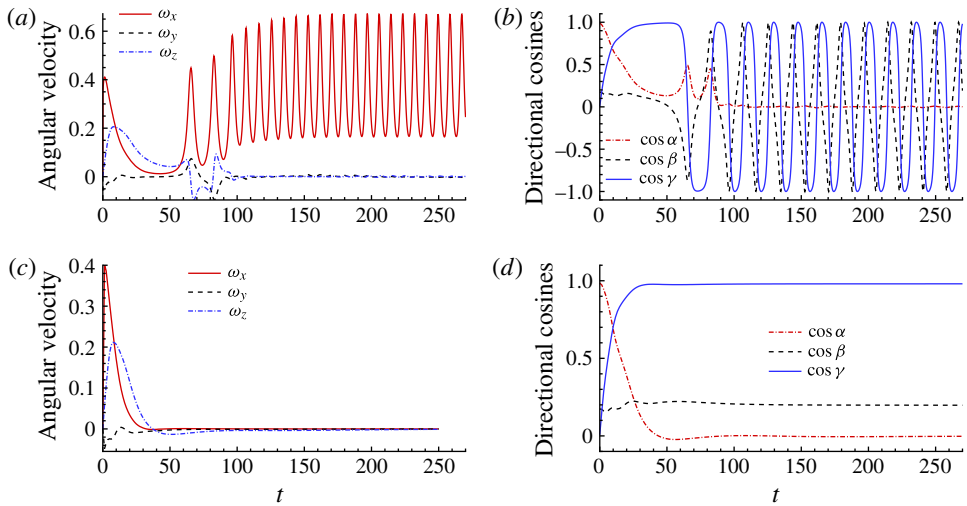

FIGURE 12. (Colour online) (*a*) Transient angular velocity and (*b*) orientation at $Re = 400$ with initial orientation (5°, 5°, 5°). The rotational mode at this Re is tumbling. (*c*) Transient angular velocity and (*d*) orientation at $Re = 500$ with initial orientation (5°, 5°, 5°). The mode at this Re is motionless.

(vii) Regime six ($385 < Re < 445$).

In this regime the tumbling mode reappears. Figure 12 shows the transient angular velocity (*a*) and orientation (*b*) for $Re = 400$. Both amplitude and frequency of ω_x are found to be close to the low-Re cases depicted in figure 6.

(viii) Regime seven ($445 < Re < 700$).

Figures 12(*c*) and 12(*d*) show the transient angular velocity and orientation for $Re = 500$, respectively. Eventually, the prolate spheroid motion stops and the axis of symmetry (i.e. x'-axis) stays almost in the (y, z)-plane. The angle between the evolution axis of the particle and the z-axis is $\sim 11°$ because $\cos\gamma = 0.98$. Figure 13 shows the pressure contours on the surface of the prolate spheroid and the (y, z)-plane when the particle is at its stationary position. It is observed that the torques produced by the pressure and shear stress on its surface are in opposite directions. In this steady mode the two imposed torques are in balance because the sum of the torques is zero. Hence, the particle will not rotate any more and keeps its steady state position.

Having reported the rotational transitions, the effects of Re on the final orientation will be addressed. In regime three, the angle between the x'-axis and (x, y)-plane (α') and the angle between the x'-axis and (x, z)-plane (δ) as functions of Re are illustrated in figure 14(*a*). We can see that the evolution axis (x'-axis) is almost in the (x, z)-plane but may have a small deviation δ from it. Because δ is very small, the value of α' is almost equal to α. α' seems negative for lower Reynolds numbers but positive for higher Reynolds numbers. Although the sign of α' appears to be chosen randomly by the flow system and the motion of the particle, the absolute values of the angles α' and δ increase monotonically with Re but α' is found not to exceed 45° for cases with $r_1 = 4$ and $r_2 = 2$.

For $Re > 445$, eventually the particle does not rotate any more and takes a stationary position in the flow field. The revolution axis of the spheroid (x'-axis) is on the (y, z)-plane because the deviations between the x'-axis and the plane are found to be below 0.5°. The angle between the x'- and z-axis (γ) as a function of Re is illustrated

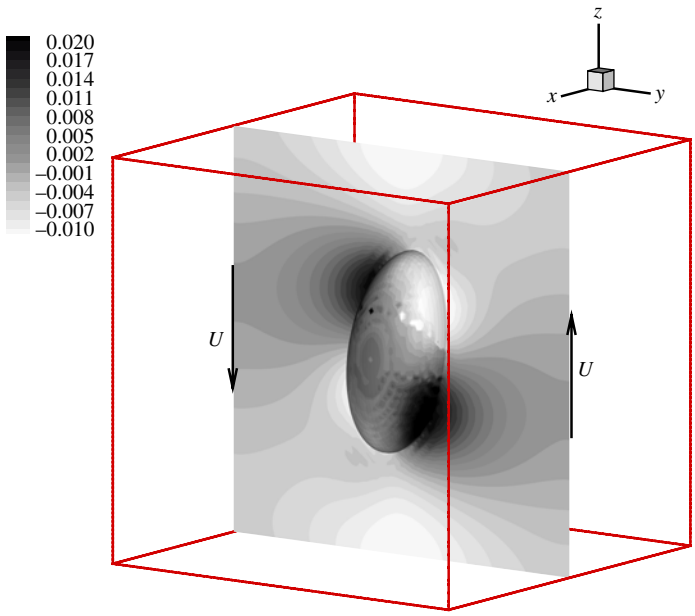

FIGURE 13. (Colour online) Pressure Δp contours on the surface of the prolate spheroid and the (y, z)-plane when the particle is at its stationary position ($Re = 500$ and initial orientation is $(5°, 5°, 5°)$). $\Delta p = (p - p_0)/(\rho_0 U^2/2)$, where $p_0 = c_s^2 \rho_0$.

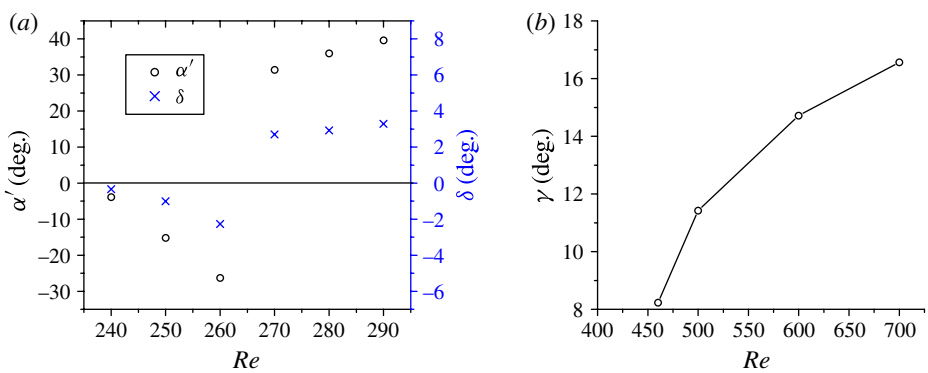

FIGURE 14. (Colour online) (*a*) The angle between the x'-axis and (x, y)-plane (α') and the angle between the x'-axis and (x, z)-plane (δ) as a function of Re; the prolate spheroid displays inclined rolling. (*b*) The angle between the x'- and z-axes (γ) as a function of Re after the prolate spheroid attains a steady mode.

in figure 14(*b*). It is observed that the angle increases monotonically with the Reynolds number up to the maximum value of $Re = 700$ studied in this work.

In the following the effects of the confinement ratio will be addressed. When r_1 is large enough (i.e. the particle diameter is small compared to the channel diameter), the two moving boundaries at $y = 0$ and $y = N_y$ would have very little effect on the rotation of the particle and thus the transition Reynolds numbers will become independent of r_1. However, such a study would not be feasible without grid refinement, which we did not implement for this study. Comparing the cases of $r_1 = 4$

Regime	*Re* range	Case	Possible final modes
1	$0 < Re < 120$	$Re = 50$	Tumbling
2	$120 < Re < 235$	$Re = 150$	Log rolling; tumbling
2		$Re = 200$	Log rolling; tumbling
3	$235 < Re < 305$	$Re = 260$	Inclined rolling; tumbling
4	$305 < Re < 345$	$Re = 310$	Precessing and nutating around an inclined axis; tumbling
5	$345 < Re < 385$	$Re = 350$	Precessing and nutating around x-axis; tumbling
6	$385 < Re < 445$	$Re = 400$	Tumbling
7	$445 < Re < 700$	$Re = 500$	Stationary; tumbling

TABLE 3. Typical modes of motion for the different regimes.

and 5 at typical *Re* in our study above, we found the rotation transitions at $r_1 = 5$ are similar to those at $r_1 = 4$. The critical *Re* at $r_1 = 5$ are slightly different from those at $r_1 = 4$. For example, for $r_1 = 5$ the first transition Reynolds number is found to be $Re \approx 105$ while *Re* is ~ 120 for $r_1 = 4$. Hence, for $r_1 = 4$ the moving boundaries at $y = 0$ and $y = N_y$ only have a minor effect on the rotation of a spheroid. For smaller r_1, due to the significant effect of the moving boundaries, the rotational transitions may be very different from the case of $r_1 = 4$.

Hence, it should be kept in mind that the specific values of the critical Reynolds numbers separating the various regimes are r_1-dependent, at least in the range of confinement ratio investigated here. A closer inspection of the velocity field indeed reveals that the wake of the particle may interact with that same particle due to the use of periodic boundary conditions (not shown here).

4.2. *Effects of initial orientation*

In this section we discuss the effects of initial orientation. For an initial orientation of $(0°, 0°, 0°)$ of the prolate spheroid, the rotational mode is always log rolling for $Re \leqslant 700$ whereas ω_x increases for higher *Re*. When the x'-axis of the prolate spheroid is initially set in the (y, z)-plane, the particle reaches a tumbling mode for all $Re < 700$. In the following discussion we exclude these special initial orientations.

Table 3 shows typical modes of motion for the different *Re* regimes. Tumbling always seems to be present even excluding the two special orientations mentioned above.

For $Re < 120$ and $385 < Re < 445$, the rotational mode would always be tumbling independent of the initial orientation. For the other regimes the final mode depends on the initial orientation. This conclusion holds for all modes of the 57 different initial orientations (shown in figure 16 below, except the special initial orientations (0, 0, 0) and x' in the (y, z)-plane).

The initial orientation effect on the final mode at $Re = 150$ and 200 is displayed in figure 15. The sphere in the figure is used to guide the eye and a diameter drawn on the sphere denotes a possible initial orientation. Each symbol on the sphere denotes an initial orientation of the minor and major axes of the oblate and prolate particle, respectively. The grid intervals in the meridian and latitude directions are both 22.5°. The squares and discs represent the initial orientations which would result in log-rolling and tumbling modes, respectively. In the cases of $Re = 150$ and 200, the regions which lead to log rolling on the surface of the spheres all look like

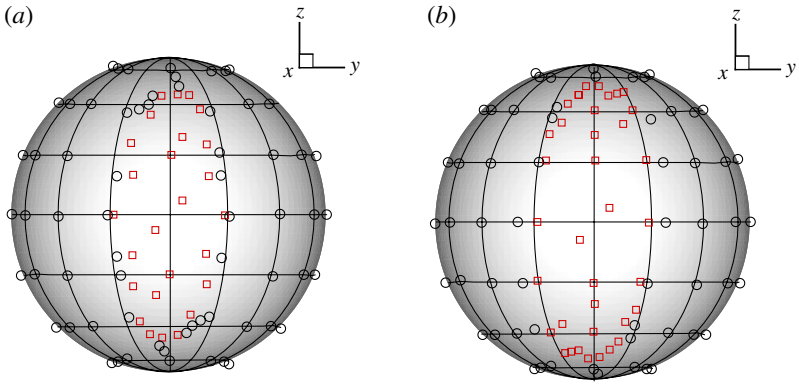

FIGURE 15. (Colour online) Initial orientation effect on the final mode at $Re = 150$ (*a*) and $Re = 200$ (*b*). The squares (□) and circles (○) denote the initial orientations which eventually reach the log-rolling and tumbling modes, respectively.

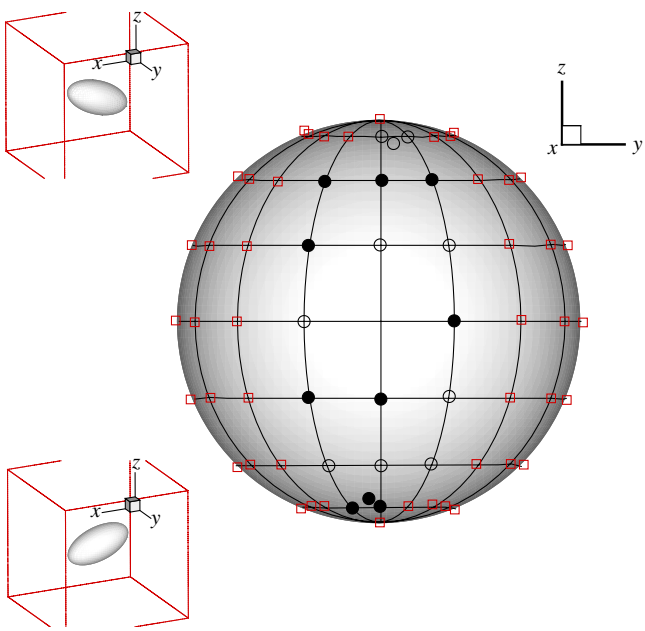

FIGURE 16. (Colour online) Initial orientation effect on the rotational mode at $Re = 260$ for a prolate spheroid. The filled circles (●), open circles (○), and squares (□) denote the initial orientations which lead to inclined rolling with a positive $\cos\gamma$ (snapshot in upper inset), inclined rolling with a negative $\cos\gamma$ (snapshot in lower inset) and tumbling mode, respectively.

ellipses projected onto the surface. We also find that the squares and circles are symmetric about the x-axis. That indicates that if two initial orientations are symmetric about the x-axis, they will reach an identical mode. For example, at $Re = 200$, the initial orientations $(-22.5°, 90°, -22.5°)$ and $(22.5°, 90°, 22.5°)$ eventually reach the same mode – log rolling – while the initial orientations $(-22.5°, 90°, 22.5°)$ and $(22.5°, 90°, -22.5°)$ both display the tumbling mode. For two cases with initial

orientations symmetric about the x-axis, the forces and torques acting on particles are also symmetric about the x-axis due to the x-axis-symmetry of Couette flow. Hence, it is reasonable to expect that the two cases will follow two symmetric orbits and finally reach an identical mode.

Comparing figures 15(*a*) and 15(*b*), we also find that the area occupied by squares seems to increase from $Re = 150$ to $Re = 200$. Hence, for a random initial orientation, the log rolling mode may have more opportunities to appear at higher Re.

In regime three, figure 16 shows the initial orientations that lead to two different modes: inclined rolling and tumbling at $Re = 260$. For the inclined rolling mode, two symmetric final orientations are possible. Snapshots of two final orientations with a positive $\cos\gamma$ and a negative $\cos\gamma$ are also illustrated on the upper and lower insets of figure 16, respectively. The sign of $\cos\gamma$ is thus determined by the initial orientation. From the distribution of the filled circles (•) and open circles (○) in figure 16, we find that when one orientation is labelled ○, its x-axis-symmetric counterpart must be labelled • and vice versa. Hence, if the two initial orientations are symmetric about the x-axis, the final orientation of the inclined rolling mode is also symmetric about the x-axis which is due to the x-axis symmetry of the Couette flow.

We conclude that for $Re = 150$, 200, and 260 the final state will be the tumbling mode when initially x' deviates far from the x-axis, i.e. the orientation closer to the (y, z)-plane which perpendicular to the vorticity axis. A similar situation is also observed at $Re = 310$, 350, 500. On the other hand, if initially x' is close to the x-axis, the periodic and motionless mode would appear at $Re = 310$, 350 and 500, respectively.

5. Rotation and orientation of an oblate spheroid

5.1. *Effects of Reynolds number*

We also carried out simulations for an oblate spheroid with Re from 0 to 520. In our numerical settings, the computational domain is $96 \times 96 \times 96$ and $a = 12$, $b = 24$, and $c = 24$. The confinement ratio is $N_y/b = 4$ and the aspect ratio $r_2 = b/a = 2$. Here x' is the revolution axis or the axis of symmetry. Similar criteria as illustrated in § 4.1 were used to identify the final mode. The critical Re to separate different regimes may have an error of ± 4.

First we studied the effects due to varying Re. Cases with different Re but identical initial orientation $(\phi_0, \theta_0, \psi_0) = (5°, 5°, 5°)$ were simulated. The final modes of the oblate spheroid are found to be simpler than those of the prolate spheroid. In the low-Reynolds-number range ($0 < Re < 112$), the oblate spheroid will eventually spin at a constant rate around the revolution axis, which is parallel to the x-axis ($\alpha = 0$). This mode is called 'spinning' (Qi & Luo 2003) or 'log rolling' (Yu *et al.* 2007). In an intermediate-Reynolds-number range ($112 < Re < 168$), the spheroid will still spin around the x'-axis. However, the revolution axis does not align with the vorticity axis (i.e. x-axis) again. It stays very close to the (x, y)-plane with $\alpha \neq 0$. This mode is called 'inclined rolling' in the study of Yu *et al.* (2007). The angle α as a function of Re is illustrated in figure 17(*a*). It increases from $\sim 10°$ to $70°$ for $120 < Re < 156$. Furthermore, we can also see that the angle between the x'-axis and (x, y)-plane (δ) is also increasing with Re although the angle amplitude is small for all cases studied.

In the higher-Reynolds-number range ($168 < Re < 520$), the spheroid will eventually stop rotating and the x'-axis will stay almost in the (y, z)-plane because the angle between x'-axis and the (y, z)-plane is less than $0.25°$ in this Reynolds number regime. The final angle β as a function of Re is illustrated in figure 17(*b*). It is observed that

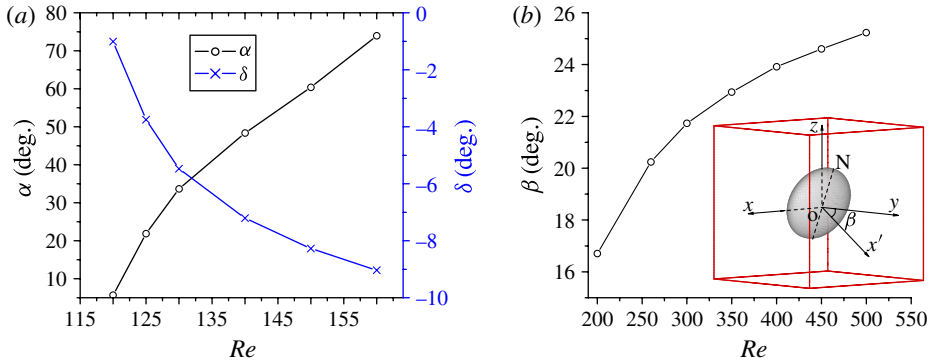

FIGURE 17. (Colour online) (*a*) The angle between x'- and x-axes (α) and the angle between the x'-axis and (x, y)-plane (δ) as a function of Re; an oblate spheroid displays inclined rolling. (*b*) The angle between the x'- and y-axes (β) as a function of Re, when the oblate spheroid takes a stationary position. The inset shows the stationary position and β at $Re = 350$. Line ON is a semi-principal axis of the oblate spheroid which is perpendicular to the x-axis. In these simulations, the initial orientations are (5°, 5°, 5°).

the value of β is increasing with Re. At the stationary position, there is a balance between the torques of the viscous force and pressure exerted on the spheroid. Our results also show that the values of torques produced by the shear force and pressure increase equally with Re. Our observation is consistent with the results of Yu *et al.* (2007) with a small discrepancy in Re because $r_1 = 5$ in their study but a value of $r_1 = 4$ is used in the present study.

In the study of Qi & Luo (2003) it was anticipated that the oblate spheroid was rotating about its major diameter which is parallel to the vorticity axis at $Re > 400$ for a random initial orientation. However, we did not observe this phenomenon. Although this tumbling mode is found in our simulations, it is limited to very special cases where x' is initially in the (y, z)-plane.

5.2. *Effects of initial orientation*

For the oblate spheroid, when the initial orientation is (0°, 0°, 0°), the final mode is always log rolling at all Re studied. We observe that those simulations where x' is set perpendicular to the vorticity direction initially would eventually reach a tumbling mode at any $Re < 520$. In the following discussion we exclude these special initial orientations.

For $Re = 100$, we observed solely the log-rolling mode for all the 57 initial orientations depicted in figure 18.

At an intermediate Reynolds number $Re = 140$, we investigated the final mode sensitivity to the initial orientation. A total of 57 cases with different initial orientations were simulated and the results are shown in figure 18. Except for the special cases mentioned above, only the inclined rolling mode exists at this Re. Figure 18 shows that the inclined x'-axis may be of a positive or a negative $\cos\beta$, which depends on the initial orientations. In this figure, the open circles (○), filled circles (●) and squares (□) denote the initial orientations which finally reach the inclined rolling with a negative $\cos\beta$ and a positive $\cos\beta$ and tumbling, respectively. Comparing two nodes symmetric about the x-axis, we find if one orientation is labelled ○, its x-axis-symmetric orientation must be labelled ● and vice versa. Hence,

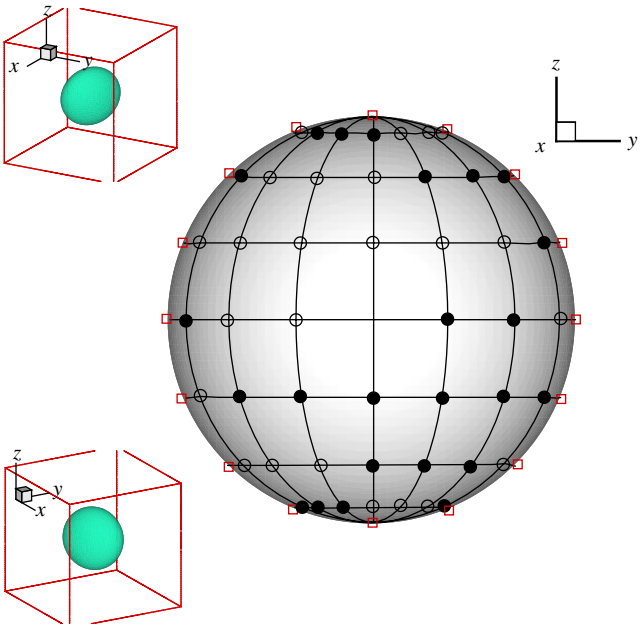

FIGURE 18. (Colour online) Initial-orientation effect on the final mode at $Re = 140$ for an oblate spheroid. The open circles (○), filled circles (●), and squares (□) denote the initial orientations which finally lead to inclined rolling with a negative $\cos\beta$ (snapshot in the lower inset), inclined rolling with a positive $\cos\beta$ (snapshot in the upper inset) and tumbling mode, respectively.

if the two initial orientations are symmetric about the x-axis, the final orientations are also symmetric about the x-axis.

For $Re > 168$ the particle will finally stop moving irrespective of its initial orientations. Thus for the oblate spheroid, the final mode appears to be insensitive to the initial orientation.

The above regime classification, modes, and effects of initial orientation for both prolate and oblate spheroids have been obtained numerically; they need to be verified in detail experimentally.

6. Energy dissipation

As mentioned in the introduction, Taylor (1923) and Feng & Joseph (1995) confirmed Jeffery's hypothesis experimentally and numerically for very small Reynolds numbers. Qi & Luo (2003) obtained some numerical results which are not consistent with Jeffery's hypothesis when they investigated the energy dissipation of a prolate spheroid in a Couette flow with $Re = 0.1$ and $Re = 18$.

Here we also investigated the energy dissipation represented by the relative viscosity π of the flow system (Qi & Luo 2003), which is given by

$$\pi = \frac{\eta_s}{\eta_f} = \frac{\langle\sigma\rangle}{\rho\nu G}, \tag{6.1}$$

where η_s and η_f are the effective suspension viscosity and solvent viscosity and $\langle\sigma\rangle$ is the average shear stress. However, Qi & Luo (2003) did not mention how

they obtained $\langle\sigma\rangle$. There are two conjectures. One may calculate $\langle\sigma\rangle$ either through averaging the shear stress over both time and the entire spheroid surface, or through averaging the shear stress acting on the moving flat wall over time directly. They are referred to as scheme 1 and scheme 2.

As we know, the shear stress in a fluid node can be obtained through $\sigma = \rho\nu(\partial_y w + \partial_z v)$, where v and w are the velocity components in the y- and z-directions, respectively. We note that in the MRT–LBM, the second-order moments of the distribution function are given by $p_{yz} = \sum_i e_{iy} e_{iz} f_i = \rho v w - \tau c_s^2 \rho(\partial_y w + \partial_z v)$. Therefore, at each fluid node the shear stress is obtained through

$$\sigma = \rho\nu\left(\partial_y w + \partial_z v\right) = \frac{\nu}{\tau c_s^2}(\rho v w - p_{yz}). \tag{6.2}$$

In the lattice Bhatnagar–Gross–Krook (BGK) method, at each fluid node the shear stress can be obtained by $\sigma = \rho\nu(\partial_y w + \partial_z v) = -(1 - (1/2\tau)) \sum f_i^{neq} \boldsymbol{e}_{iy} \boldsymbol{e}_{iz}$, where $f_i^{neq} = f_i - f_i^{eq}$.

To calculate $\langle\sigma\rangle$, a third option is a strictly volumetric average of (6.2), which should be equivalent to scheme 2. In the following simulations, we found scheme 1 is wrong. Hence we mainly discuss scheme 2. In scheme 2, through integration the shear stress on the moving flat wall, we obtained the drag force acting on the flat wall. The shear stress acting on a moving wall node is equal to that acting on the fluid node that is nearest to the wall node. Then the spatial-averaged shear stress is equal to the drag force divided by area of the moving flat wall. After the shear stress is further averaged by time, $\langle\sigma\rangle$ is obtained.

To validate scheme 2, suspensions of spherical particles in a shear flow were simulated. The numerical results were compared with Einstein's theory on a dilute suspension of spheres (Einstein 1905). According to Einstein's theory, the relative viscosity in dilute suspensions of spheres is (Einstein 1905) $\pi = 1 + \phi[\eta]$, where ϕ is the solid volume fraction, and $[\eta] = \frac{5}{2}$ is the intrinsic viscosity.

In our simulations, mesh size is $100 \times 100 \times 100$, $\tau = 1.0$ and Re is fixed to be 0.5. Two cases with radii of a spherical particle $r = 15$ and 17 were simulated, with solid volume fractions 1.41 % and 2.06 %, respectively. They can be regarded as dilute suspensions. According to scheme 1, our result shows that the calculated $[\eta] = 1.606$ and 1.297, respectively for the two cases. The values are significantly different from $\frac{5}{2}$. Hence this scheme seems not correct. For scheme 2, the result shows that the corresponding calculated $[\eta]$ values are 2.585 and 2.540, respectively, consistent with Einstein's viscosity formula. Using scheme 2, cases with different volume fractions were simulated. The relative viscosity as a function of ϕ is shown in figure 19. Our LBM result agrees well with Einstein's theory when ϕ is small. Hence scheme 2 is able to give accurate results.

Once the scheme of calculating relative viscosity was validated, we studied the relative viscosity of the flow system for a prolate and oblate spheroid with and without constraints. In these simulations, mesh size is $96 \times 96 \times 96$ and $\tau = 1.0$. The results are listed in table 4. Here π_1 and π_2 are the relative viscosity for the log-rolling and tumbling modes, respectively. For the prolate spheroid cases, the log rolling mode is initiated by fixing the x'-axis (evolution axis) in the x-direction and the tumbling mode is the mode due to an unconstrained motion of the spheroid. From the table we can see that the relative viscosity increase with Re for a given dynamical mode. For the prolate case, the solid volume fraction is approximately $\phi = 1.64$ %. Through formula $[\eta] = (\pi - 1)/\phi$, we can identify that for the case of $Re = 0.1$, the intrinsic viscosities are 2.181 and 2.844 for the log-rolling and tumbling mode, respectively. Jeffery (1922)

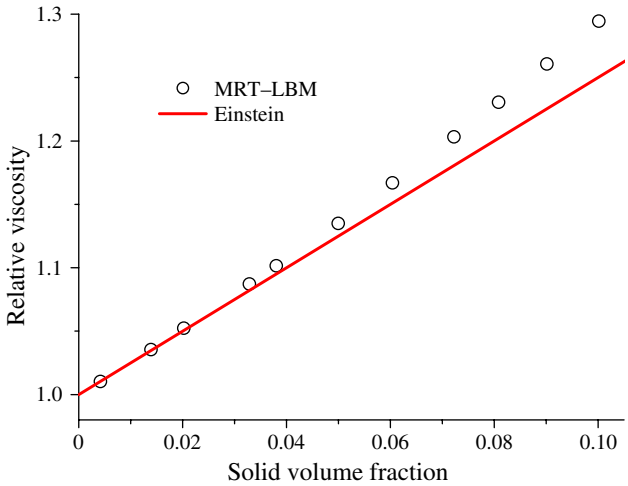

FIGURE 19. (Colour online) Relative viscosity of a suspension of spherical particles as a function of the volume fraction ϕ. Circles denote our MRT–LBM result ($Re = 0.5$). The solid line denotes Einstein's shear viscosity formula for a dilute suspension as $Re \to 0$.

has given the range of $[\eta]$ for a prolate spheroid with different aspect ratios. For our cases (aspect ratio $a/b = 2$), the range of $[\eta]$ is $2.174 \leqslant [\eta] \leqslant 2.819$ (Jeffery 1922). Here we can see that calculated $[\eta]$ for the two modes is consistent with the minimum and maximum $[\eta]$ given by Jeffery (1922). We also found that the tumbling mode without any constraint is not the mode with a minimum dissipation of energy. This result invalidates Jeffery's hypothesis.

For the oblate spheroid cases, the tumbling mode was excited by setting the initial orientation as $(0°, 90°, 90°)$. From the table, we can see the relative viscosity in the tumbling mode is less than that in the log-rolling mode. For a unconstrained oblate spheroid, at these Reynolds numbers, the asymptotic mode is log rolling. Hence, for this oblate spheroid case, the log-rolling mode does not have a smaller energy dissipation than the tumbling mode. Therefore, our results for the oblate spheroid at small Re invalidate Jeffery's hypothesis. For the oblate cases, the solid volume fraction is approximately $\phi = 3.27\,\%$. At $Re = 0.1$, the intrinsic viscosities are 3.442 and 2.331 for the log-rolling and tumbling mode, respectively. The intrinsic viscosities are consistent with the maximum and minimum $[\eta]$ given by Jeffery (1922) for the oblate spheroid, i.e. 3.267 and 2.306.

7. Conclusions

The rotation of a neutrally buoyant spheroidal particle in a Couette flow is studied using MRT–LBM with $Re \leqslant 700$. Compared with the previous LBM, the present scheme is able to handle a curved-wall boundary more accurately and improve numerical stability at higher Reynolds number.

Seven rotational transitions are found for the prolate spheroid for $Re < 700$. The first transition Re_c from the tumbling mode to the log-rolling mode is found to be 120. The Re_c found by Qi & Luo (2003) is $\sim$205 for confinement ratio $r_1 = 4$. However, whether their conclusion is applicable to initial orientation $(5°, 5°, 5°)$ is unknown because their initial orientation is very different from ours. Obviously the transitional Re_c depends on the initial orientation. Yu *et al.* (2007) obtained the

Spheroid	Re	π_1 (log-rolling mode)	π_2 (tumbling mode)	Final mode (unconstrained)
Prolate	0.1	1.03568	1.04653	Tumbling
Prolate	1.0	1.03568	1.04655	Tumbling
Prolate	10.0	1.03615	1.04723	Tumbling
Prolate	18.0	1.03689	1.04834	Tumbling
Oblate	0.1	1.11266	1.07631	Log rolling
Oblate	1.0	1.11268	1.07741	Log rolling
Oblate	10.0	1.11428	1.07868	Log rolling
Oblate	18.0	1.11724	1.08060	Log rolling

TABLE 4. Relative viscosity of the flow system for spheroids with and without constraints.

transition $Re_c \approx 160$ for $r_1 = 5$ with a initial orientation $(0°, 90°, 45°)$ using the FD scheme. What the transitional Re_c is for the initial orientation $(5°, 5°, 5°)$ and $r_1 = 4$ is unknown. We ran the cases with $(\phi_0, \theta_0, \psi_0) = (0°, 90°, 45°)$ and $r_1 = 5$ but we found $Re_c \approx 120$. Hence, there is a discrepancy between our result and that of Yu *et al.* (2007). A possible reason is that the fluid–solid coupling scheme is different. Our coupling scheme is explicit (Aidun *et al.* 1998) while their scheme (Yu *et al.* 2007) is implicit. To the best of our knowledge, a direct comparison between different coupling schemes is not available in the literature.

In our study the transition Re_{c2} from the tumbling mode to log rolling is $\sim$235, which is consistent with the result of Yu *et al.* (2007) although in their study $r_1 = 5$ and $(\phi_0, \theta_0, \psi_0) = (0°, 90°, 45°)$. However, Qi & Luo (2003) found $Re_{c2} \approx 345$ but the initial orientation is unknown, which is not consistent with ours and that of Yu *et al.* (2007). The prolate spheroid transitioned to the inclined rolling mode (Reynolds number regime *three*) at $Re > Re_{c2}$.

Besides above mode transitions, we found periodic modes of precessing and nutating around an inclined axis and the x-axis in Reynolds number regimes *four* and *five*, respectively, for the prolate spheroid in Couette flow. The steady stationary mode for $Re > 445$ for the prolate spheroid is being reported for the first time.

The rotational transitions for the oblate spheroid are simpler than those for the prolate spheroid. In the present study, only two transitions are found for the oblate spheroid for $Re < 520$. The first and second transition Reynolds numbers are $Re'_{c1} = 112$ and $Re'_{c2} = 168$, respectively for $(\phi_0, \theta_0, \psi_0) = (5°, 5°, 5°)$. Yu *et al.* (2007) reported $Re'_{c1} \in (89.6, 128)$ and $Re'_{c2} \in (128, 160)$ for $r_1 = 5$ and $(\phi_0, \theta_0, \psi_0) = (45°, 0°, 0°)$. Our results are consistent with those obtained by Yu *et al.* (2007). However, in the study of Qi & Luo (2003), only one transition from log rolling to inclined rolling at $Re_c \approx 220$ was observed and the oblate particle did not stop rotating. This is not consistent with our result and that of Yu *et al.* (2007). In the case of inclined rolling, the inclined angle represented by α is monotonically increasing with Re both for the prolate and oblate spheroids.

The effects of initial orientation were studied for both prolate and oblate spheroids. When the initial orientation is $(0, 0, 0)$, the asymptotic mode is always log rolling. When initially the x'-axis is set in the (y, z)-plane, the tumbling mode will occur independently of Re. Except for these special cases and based on the observation of 57 initial orientations, we found only the tumbling mode for the prolate spheroid for $Re < 120$ and $385 < Re < 445$. In other Re regimes, the final mode is sensitive to the

initial orientation. However, the oblate spheroid dynamics is insensitive to its initial orientation.

During the investigation of energy dissipation at low Reynolds numbers we found that the final mode without constraints does not have a lower energy dissipation than that of the mode which is tentatively constrained. Here at $Re \approx 1$, our results also invalidate Jeffery's hypothesis (Jeffery 1922): 'The particle will tend to adopt that motion which, of all the motions possible under the approximated equations, corresponds to the least dissipation of energy'.

In the future we will carry out studies on rotational and translational behaviour of spheroidal particles in complex flows.

Acknowledgements

H.H. is grateful to anonymous referees, who gave us constructive suggestions to test our scheme for calculating the average shear stress in § 6 (energy dissipation). The sincere suggestions improved the quality of the paper. H.H. is also grateful to Professor L.-S. Luo, who took much time in reading this manuscript and provided many good suggestions. We acknowledge helpful discussions with Dr D. Qi. H.H. is supported by the Alexander von Humboldt Foundation, Germany. This work was also partially supported by National Natural Science Foundation of China (NSFC) (Grant No. 11172297).

Appendix. Matrix $\boldsymbol{M}$

The transformation matrix $\boldsymbol{M}$ used in the LBM to map a vector in discrete velocity space to moment space is (d'Humiéres *et al.* 2002):

$$\begin{pmatrix}
1 & 1 & 1 & 1 & 1 & 1 & 1 & 1 & 1 & 1 & 1 & 1 & 1 & 1 & 1 & 1 & 1 & 1 & 1 \\
-30 & -11 & -11 & -11 & -11 & -11 & -11 & 8 & 8 & 8 & 8 & 8 & 8 & 8 & 8 & 8 & 8 & 8 & 8 \\
12 & -4 & -4 & -4 & -4 & -4 & -4 & 1 & 1 & 1 & 1 & 1 & 1 & 1 & 1 & 1 & 1 & 1 & 1 \\
0 & 1 & -1 & 0 & 0 & 0 & 0 & 1 & -1 & 1 & -1 & 1 & -1 & 1 & -1 & 0 & 0 & 0 & 0 \\
0 & -4 & 4 & 0 & 0 & 0 & 0 & 1 & -1 & 1 & -1 & 1 & -1 & 1 & -1 & 0 & 0 & 0 & 0 \\
0 & 0 & 0 & 1 & -1 & 0 & 0 & 1 & 1 & -1 & -1 & 0 & 0 & 0 & 0 & 1 & -1 & 1 & -1 \\
0 & 0 & 0 & -4 & 4 & 0 & 0 & 1 & 1 & -1 & -1 & 0 & 0 & 0 & 0 & 1 & -1 & 1 & -1 \\
0 & 0 & 0 & 0 & 0 & 1 & -1 & 0 & 0 & 0 & 0 & 1 & 1 & -1 & -1 & 1 & 1 & -1 & -1 \\
0 & 0 & 0 & 0 & 0 & -4 & 4 & 0 & 0 & 0 & 0 & 1 & 1 & -1 & -1 & 1 & 1 & -1 & -1 \\
0 & 2 & 2 & -1 & -1 & -1 & -1 & 1 & 1 & 1 & 1 & 1 & 1 & 1 & 1 & -2 & -2 & -2 & -2 \\
0 & -4 & -4 & 2 & 2 & 2 & 2 & 1 & 1 & 1 & 1 & 1 & 1 & 1 & 1 & -2 & -2 & -2 & -2 \\
0 & 0 & 0 & 1 & 1 & -1 & -1 & 1 & 1 & 1 & 1 & -1 & -1 & -1 & -1 & 0 & 0 & 0 & 0 \\
0 & 0 & 0 & -2 & -2 & 2 & 2 & 1 & 1 & 1 & 1 & -1 & -1 & -1 & -1 & 0 & 0 & 0 & 0 \\
0 & 0 & 0 & 0 & 0 & 0 & 0 & 1 & -1 & -1 & 1 & 0 & 0 & 0 & 0 & 0 & 0 & 0 & 0 \\
0 & 0 & 0 & 0 & 0 & 0 & 0 & 0 & 0 & 0 & 0 & 0 & 0 & 0 & 0 & 1 & -1 & -1 & 1 \\
0 & 0 & 0 & 0 & 0 & 0 & 0 & 0 & 0 & 0 & 0 & 1 & -1 & -1 & 1 & 0 & 0 & 0 & 0 \\
0 & 0 & 0 & 0 & 0 & 0 & 0 & 1 & -1 & 1 & -1 & -1 & 1 & -1 & 1 & 0 & 0 & 0 & 0 \\
0 & 0 & 0 & 0 & 0 & 0 & 0 & -1 & -1 & 1 & 1 & 0 & 0 & 0 & 0 & 1 & -1 & 1 & -1 \\
0 & 0 & 0 & 0 & 0 & 0 & 0 & 0 & 0 & 0 & 0 & 1 & 1 & -1 & -1 & -1 & -1 & 1 & 1
\end{pmatrix} \tag{A 1}$$

REFERENCES

AIDUN, C. K., LU, Y. & DING, E. 1998 Direct analysis of particulate suspensions with inertia using the discrete Boltzmann equation. *J. Fluid Mech.* **373**, 287–311.

BOUZIDI, M., FIRDAOUSS, M. & LALLEMAND, P. 2001 Momentum transfer of a Boltzmann-lattice fluid with boundaries. *Phys. Fluids* **13**, 3452–3459.

BRADY, J. F. & BOSSIS, G. 1988 Stokesian dynamics. *Annu. Rev. Fluid Mech.* **20**, 111–157.

DING, E. & AIDUN, C. K. 2000 The dynamics and scaling law for particles suspended in shear flow with inertia. *J. Fluid Mech.* **423**, 317–344.

EINSTEIN, A. 1905 Investigations on the theory of Brownian movement. *Ann. Phys.* **17**, 549–560.

FENG, J. & JOSEPH, D. D. 1995 The unsteady motion of solid bodies in creeping flows. *J. Fluid Mech.* **303**, 83–102.

FENG, Z.-G. & MICHAELIDES, E. E. 2004 The immersed boundary-lattice Boltzmann method for solving fluid-particles interaction problems. *J. Comput. Phys.* **195**, 602–628.

GUO, Z. L., ZHENG, C. G. & SHI, B. C. 2002 An extrapolation method for boundary conditions in lattice Boltzmann method. *Phys. Fluids* **14**, 2007–2010.

HARPER, E. Y. & CHANG, I.-D. 1968 Maximum dissipation resulting from lift in a slow viscous shear flow. *J. Fluid Mech.* **33**, 209–225.

HE, X., ZOU, Q., LUO, L.-S. & DEMBO, M. 1997 Analytic solutions of simple flows and analysis of non-slip bundary conditions for the lattice Boltzmann BGK model. *J. Stat. Phys.* **87**, 115–136.

D'HUMIÉRES, D., GINZBURG, I., KRAFCZYK, M., LALLEMAND, P. & LUO, L.-S. 2002 Multiple-relaxation-time lattice Boltzmann models in three dimensions. *Phil. Trans. R. Soc. Lond.* A **360**, 437–451.

JEFFERY, G. B. 1922 The motion of ellipsoidal particles immersed in a viscous fluid. *Proc. R. Soc. Lond.* A **102**, 161–179.

KARNIS, A., GOLDSMITH, H. L. & MASON, S. G. 1963 Axial migration of particles in Poiseuille flow. *Nature* **200**, 159–160.

LADD, A. J. C. 1994*a* Numerical simulations of particulate suspensions via a discretized Boltzmann equation. Part 1. Theoretical foundation. *J. Fluid Mech.* **271**, 285–309.

LADD, A. J. C. 1994*b* Numerical simulations of particulate suspensions via a discretized Boltzmann equation. Part 2. Numerical results. *J. Fluid Mech.* **271**, 311–339.

LALLEMAND, P. & LUO, L.-S. 2003 Lattice Boltzmann method for moving boundaries. *J. Comput. Phys.* **184**, 406–421.

LEAL, L. G. 1975 The low motion of slender fluid rod-like particles in a second order fluid. *J. Fluid Mech.* **69**, 305–337.

LEAL, L. G. 1980 Particle motion in a viscous fluid. *Annu. Rev. Fluid Mech.* **12**, 435–476.

MEI, R., YU, D., SHYY, W. & LUO, L.-S. 2002 Force evaluation in the lattice Boltzmann method involving curved geometry. *Phy. Rev.* E **65**, 041203.

QI, D. 1999 Lattice-Boltzmann simulations of particles in non-zero-Reynolds-number flows. *J. Fluid Mech.* **385**, 41–62.

QI, D. & LUO, L.-S. 2002 Transitions in rotations of a non-spherical particle in a three-dimensional moderate Reynolds number Couette flow. *Phys. Fluids* **14**, 4440–4443.

QI, D. & LUO, L.-S. 2003 Rotational and orientational behaviour of a three-dimensional spheroidal particles in Couette flows. *J. Fluid Mech.* **477**, 201–213.

TAYLOR, G. I. 1923 The motion of ellipsoidal particles in a viscous fluid. *Proc. R. Soc. Lond.* A **102**, 58–61.

YU, Z., PHAN-THIEN, N. & TANNER, R. I. 2007 Rotation of a spheroid in a Couette flow at moderate Reynolds numbers. *Phys. Rev.* E **76**, 026310.

ZETTNER, C. M. & YODA, M. 2001 Moderate-aspect-ratio elliptical cylinders in simple shear with inertia. *J. Fluid Mech.* **442**, 241–266.